Topology of 2-D turbulent structures based on intermittence in the TJ-II stellarator

B.Ph. van Milligen[1], A.V. Melnikov[2], B.A. Carreras[3], L. García[3], A.S. Kozachek[4], C. Hidalgo[1], J.L. de Pablos[1], P.O. Khabanov[2], L.G. Eliseev[2], M.A. Drabinskiy[2], A. Chmyga[4], L. Krupnik[4], the HIBP Team, the TJ-II Team

[1] National Fusion Laboratory, CIEMAT, Avda. Complutense 40, 28040 Madrid, Spain

[2] NRC 'Kurchatov Institute', 123182, Moscow, Russia

[3] Departamento de Física, Universidad Carlos III, Avda. de la Universidad 30, 28911 Leganés, Spain

[4] Institute of Plasma Physics, NSC KIPT, 310108, Kharkov, Ukraine

Abstract. This work estimates the degree of turbulent intermittence of the plasma potential measured by a Heavy Ion Beam Probe in the core plasma region of the TJ-II stellarator. It is shown that the intermittence varies in a significant way with the plasma state (ion or electron root). In addition, radial minima of the intermittence are found to be associated with the location of topological structures of the flow associated with some important low-order rational surfaces. The local pressure gradient was also estimated, and a clear correlation was found between the steepening of the pressure gradient and the deepening of the minima of the intermittence, suggesting that the minima are associated with pressure gradient driven modes.

By estimating the rotation velocity of the plasma from the measured plasma potential, it was possible to make a rough reconstruction of the twodimensional radial-poloidal map of intermittence, thus clarifying the topological structure of the intermittence. The experimental results were put into context by comparing with simulations performed using a resistive Magneto-Hydrodynamic turbulence model.

1. Introduction

Our knowledge of magnetically confined plasmas has improved significantly over the years, and the large scale radial structure is generally well understood, mainly on the basis of Neoclassical Theory. This understanding has been driven by the availability of diagnostics that reveal the mean radial structure ('profiles') of quantities like electron and ion density, temperature, and pressure.

However, magnetically confined plasmas are strongly driven, complex, self-organized systems, far from thermodynamic equilibrium. Turbulence is known to play a major role in phenomena like self-organization, profile resilience (or 'consistency'), power degradation, and transient rapid transport phenomena [1] – and therefore, turbulence will affect the scaling of confinement properties and the design of future reactor systems in a significant way [2]. A proper quantification of turbulence requires going beyond simple linear and local measures such as the turbulent amplitude or its spectrum, due to the fact that turbulence and background profiles interact mutually in nonlinear feedback loops, and that turbulence is a phenomenon that cannot be treated as 'local' due to the rapid long-range effects it sometimes produces [3].

Experimental data on turbulence are difficult to obtain in the interior of a hot plasma [4, 5, 6]. This implies that our knowledge on turbulence in the core region is incomplete, relying heavily on turbulence simulations and simplifying assumptions. It has been shown, however, that existing diagnostic data sometimes contain very interesting information on core turbulence that can be extracted by means of advanced analysis techniques. As an example, by making use of an analysis based on the Transfer Entropy and applying it to Electron Cyclotron Emission (ECE) data we have recently shown that electron heat transport is far from diffusive in the plasma core under ECRH conditions [7]. In any case, further studies of core plasma turbulence are vital to complete our picture of transport in magnetically confined plasmas.

Here, we focus on the intermittence parameter $C(1)$, a quantity originating in chaos theory that allows measuring the degree of multifractality of fluctuating signals [8][9]. This parameter is related to the rate of turbulent dissipation and the fractal dimension of the underlying dynamics. Hence, this quantity is of prime importance in turbulence studies. For reference, we note that in the past, the degree of intermittence has been studied using the 'flatness factor' [10], which is a quantifier of the shape of the probability distribution function of the fluctuating variable that does not take the actual time-varying properties of the variable into account; whereas $C(1)$ does, explaining why the latter is a more powerful and precise quantifier of turbulent dissipation.

In the year 2000, this intermittence parameter was calculated for the first time for data from magnetically confined plasmas, by analyzing Langmuir probe measurements obtained in the plasma edge region [11]. This line of investigation was not pursued further for twenty years, but when core ECE fluctuation data from the W7-X stellarator became available and the mentioned studies based on the Transfer Entropy had previously shown the presence of interesting radial structures of heat transport [12],

it was resumed and successfully applied to these data, providing the first measurements of intermittence in the core plasma region [13]. Next, the analysis was again applied to Langmuir probe data from TJ-II, this time in experiments carefully designed to study the effect of rational surfaces by performing slow scans of the rotational transform [14].

The latter two studies revealed that intermittence offers an interesting way to study plasma turbulence and understand the impact of low-order rational surfaces on turbulence. Near dominant low order rational surfaces, modes with the corresponding helicity tend to dominate fluctuations, leading to a local reduction of the degree of multifractality. On the other hand, strong plasma rotation may lead to the mixing of the local fluctuations with variations associated with the poloidal structure of modes, leading to an increase of multifractality. Hence, the intermittence parameter is sensitive to the presence of both low-order rational surfaces and poloidal flows (such as zonal flows). Therefore, this analysis technique provides one of the few ways to explore turbulent structure in the core region of magnetically confined plasmas.

In the present work, these studies are extended further by applying the technique to core data obtained by the Heavy Ion Beam Probe (HIBP) system at TJ-II. A Resistive Magneto-HydroDynamical (R-MHD) turbulence model is used to facilitate interpretation of the results.

The structure of this paper is as follows. In Section 2, the TJ-II device, its HIBP system, the intermittence and its interpretation, and the R-MHD turbulence model are briefly described. In Section 3, the experimental data and the analysis results are presented, and Section 4 shows some results for turbulence calculations based on the R-MHD model. Section 5 presents a discussion, putting the results into context, comparing experimental and modeling results, offering an interpretation and drawing some conclusions.

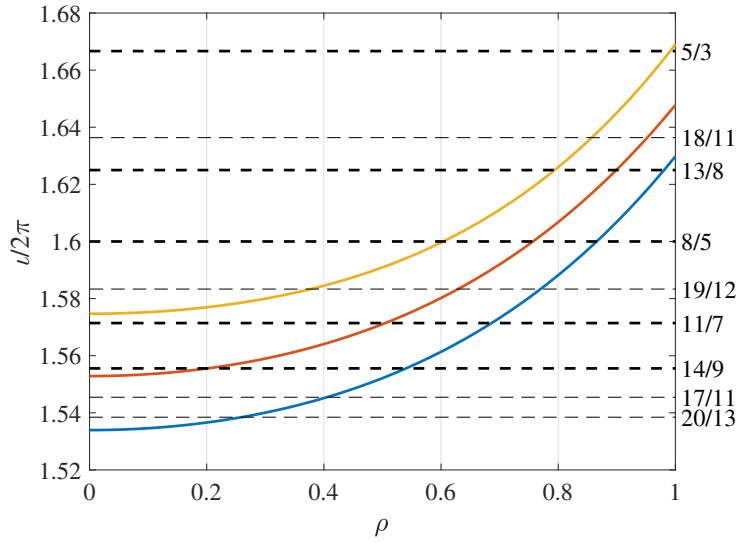

Figure 1. Rotational transform profiles for three magnetic configurations, labelled '100_42_63' (bottom), '100_44_64' (middle) and '100_46_65' (top). Some rational values are indicated by means of horizontal dashed lines.

2. Methods

2.1. TJ-II

The experiments discussed here have been performed at TJ-II, a flexible Heliac with toroidal magnetic field $B_T \simeq 1$ T, major radius $R_0 = 1.5$ m and minor radius $a < 0.22$ m [15]. Plasmas can be heated using two Electron Cyclotron Resonance Heating (ECRH) beam lines delivering up to 300 kW each at a frequency of 53.2 GHz (X mode) and two Neutral Beam Injector (NBI) systems (co and counter) with up to 2×700 kW port-through power. In this work, we limit ourselves to ECRH plasmas.

TJ-II ECRH plasmas exhibit a spontaneous transition from electron root confinement to ion root confinement, typically occurring at a line average electron density of $\overline{n_e} \simeq 0.6 \cdot 10^{19}$ m^{-3} [16, 17]. This transition is characterized by a change of sign of the radial electric field E_r in the edge region.

We will analyze discharges in various closely similar magnetic configurations, with slightly differing locations of rational surfaces (cf. Fig. 1). Due to the fact that both plasma pressure and internal plasma currents are quite small, the magnetic configuration closely matches the externally imposed configuration. In particular, the rotational transform (ι) profiles in the experimental situation are very close to the vacuum ι profiles, thus allowing the localization of low-order rational surfaces with good confidence, as discussed in more detail in previous work [18].

2.2. Heavy Ion Beam Probe

Currently, TJ-II disposes of two Heavy Ion Beam Probe (HIBP) systems, located at equivalent toroidal angles of 219° (system I) and 129° (system II) [19]. However, the analysis presented here reexamines data of experiments performed in 2008 and only makes use of data from the slightly older system I.

The system injects accelerated Cs^+ ions into the plasma and captures secondary Cs^{2+} ions in an energy analyzer. The energy of the secondary ions provides information about the plasma potential Φ in the sample volume of the ion beam, the beam current $I_{\rm tot}$ provides information about the local electron density n_e, and the toroidal displacement of the beam Z_c provides information about the poloidal current density in the plasma. Traveling through the plasma, the beam experiences attenuation, affecting $I_{\rm tot}$ [20].

The beam can be actively steered, so that the beam sample volume can be scanned through the plasma, from the High Field Side (HFS) to the Low Field Side (LFS) and back in the corresponding poloidal cross section. The swept sample volume does not necessarily cross the magnetic axis. By performing beam tracing calculations, the position of the sample volume can be recovered, expressed in terms of the normalized radius of the known magnetic configuration.

The beam tracing calculations also allow estimating the size of the sampling volume, which is typically around 1–2 cm poloidally and somewhat less radially. The bandwidth of the data acquisition preamplifiers is 1 MHz, sufficient to study plasma turbulence.

2.3. Intermittence

The intermittence parameter arises in the field of chaos theory [8][9]. The fluctuation level of a time series of length N is characterized by its normalized root-mean-quare (RMS) value ϵ, calculated over sub-time windows with length $n \leq N$: $\epsilon = {\rm RMS}_n/{\rm RMS}_N$. The moments $\langle \epsilon^{\mathbb{q}} \rangle$, averaged over all available sub-windows with length n, are expected to decay as a power of the window length, namely $\langle \epsilon^{\mathbb{q}} \rangle \propto n^{-K(\mathbb{q})}$. When K is linear in $\mathbb{q}$, the time series is considered to be monofractal, otherwise it is multifractal. The intermittence parameter $C(1)$ is defined as the derivative $dK/d\mathbb{q}$ evaluated at $\mathbb{q} = 1$, and ranges from 0 for a monofractal time series to 1 for a multifractal time series. Please refer to Appendix A for more details.

The calculation of the intermittence parameter $C(1)$ is rather insensitive to random noise. To test this statement, we have taken an experimental time series with varying values of $C(1)$, added random Gaussian noise to it, and recalculated $C(1)$. Fig. 2 shows the standard deviation between the recalculated value of $C(1)$ and the value of $C(1)$ from the original data. The amplitude of the additive noise is expressed as a percentage of the RMS value of the data. Even for noise levels as high as 100%, $C(1)$ varies by less than 10% from its value without noise, attesting to the robustness of the calculation.

The interpretation of the intermittence parameter has been clarified in some detail in previous work, based on R-MHD turbulence simulations (see Section 2.4 below) [13]. We summarize the main points here for convenience.

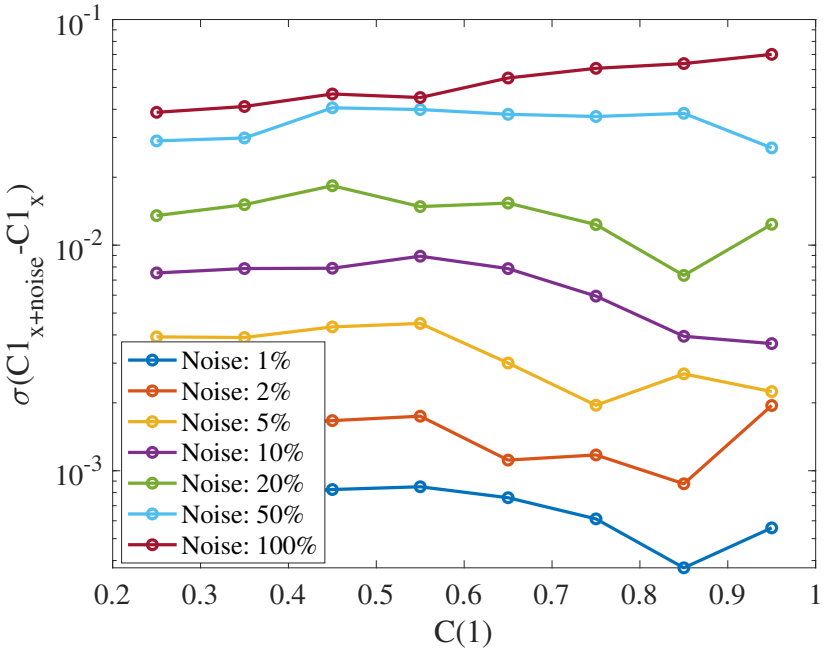

Figure 2. Standard deviation between $C(1)$ calculated from data $x(t)$ with added random Gaussian noise, and $C(1)$ calculated from data $x(t)$ without added noise. The horizontal axis specifies the value $C(1)$ of the data without noise. The noise amplitude is expressed as a percentage of the RMS value of the data $x(t)$.

$C(1)$ quantifies a property ('the degree of multifractality') of the fluctuations of a given variable, such as the electric potential or electron density, and results will differ according to the variable studied. It is known that $C(1)$ is low ($\simeq 0$) when fluctuations are dominated by a single helicity corresponding to a given rational surface; elsewhere, $C(1)$ tends to be higher due to a mixing of the effects due to multiple modes, as studied in previous work [13]. Hence, radial minima of $C(1)$ tend to coincide roughly with the location low order rational surfaces, if a mode with corresponding helicity is dominant.

The eigenmodes corresponding to a rational surface have a radial structure, such that some of these modes peak at the radial location of the rational surface, whereas others have zero amplitude at that location and peak slightly inward and/or outward from that location. The radial mode structure depends on the helical mode numbers (m and n) and the local shear, such that the mode is narrower for high mode numbers and high shear. Therefore, the correlation between the position of the minima of $C(1)$ and the location of the rational surface will be better for higher mode numbers and higher shear. Lower order modes, however, tend to dominate over higher order modes, so that this correlation with the radial location will tend to be only approximate.

The turbulence associated with low order rational surfaces may lead to the formation of vortical structures (which one may think of as filaments or island seeds) with the corresponding helicity. Within these structures, particles are 'trapped', plasma dynamics are dominated by the single corresponding helicity and $C(1)$ is low. Therefore,

minima of $C(1)$ will tend to be associated with such vortical structures.

The determination of $C(1)$ requires a certain length of data for good statistics. Typically, the plasma rotates poloidally (and/or toroidally) during the measurement time, so that the measured $C(1)$ corresponds to a mixture of the temporal fluctuation characteristics and the poloidal structure of the turbulence. The degree of mixture will depend on the properties of the diagnostic system, the data analysis settings, and local plasma rotation. In the present paper, we study plasma core fluctuations using relatively rapid scans, in an attempt to prioritize the spatial structure over the temporal structure.

2.4. Resistive MHD model

To facilitate the interpretation of the experimental observations, we will compare the latter to calculations performed with a Resistive MHD turbulence model which has been used in the past for this purpose [21, 14, 22]. The model is based on the reduced MHD equations and evolves the magnetic flux, the vorticity, the density and the temperature in a threedimensional volume [23]. TJ-II plasmas are modeled in periodic cylinder geometry, taking the rotational transform and curvature of the corresponding TJ-II configuration into account. Calculations are performed in background equilibrium conditions reproducing the specific equilibrium temperature and density profiles of the concerned discharges. The dominant instability considered is the resistive pressure gradient driven instability. Thus, the numerical calculations do not constitute a full and detailed simulation of these TJ-II plasmas, although they reproduce many of their features. Please refer to the cited references for more details.

3. Experimental results

We analyze a set of discharges in which HIBP I was scanned fast (5 ms per scan). These discharges have been analyzed in previous work, using profile data from the HIBP and fluctuations from Langmuir probes in the edge [16]. A further study was made based on information on MHD activity from Mirnov pick-up coils and poloidal flow measurements from Doppler reflectometry [24]. Thus, this set of discharges, corresponding to various magnetic configurations, has been thoroughly analyzed in the past, facilitating the interpretation of the new information presented below. In this work, we focus on the spatiotemporal structure of turbulent intermittence from the HIBP data, revealing the existence of persistent structures in the core plasma.

Fig. 3 shows a typical example of HIBP data. The figure is meant to clarify the scanning operation: the bottom panel shows the radial location of the scanned sampling volume in time, while the top panel shows the measured plasma potential Φ and the middle panel the beam current $I_{\rm tot}$ (proportional to the local electron density n_e).

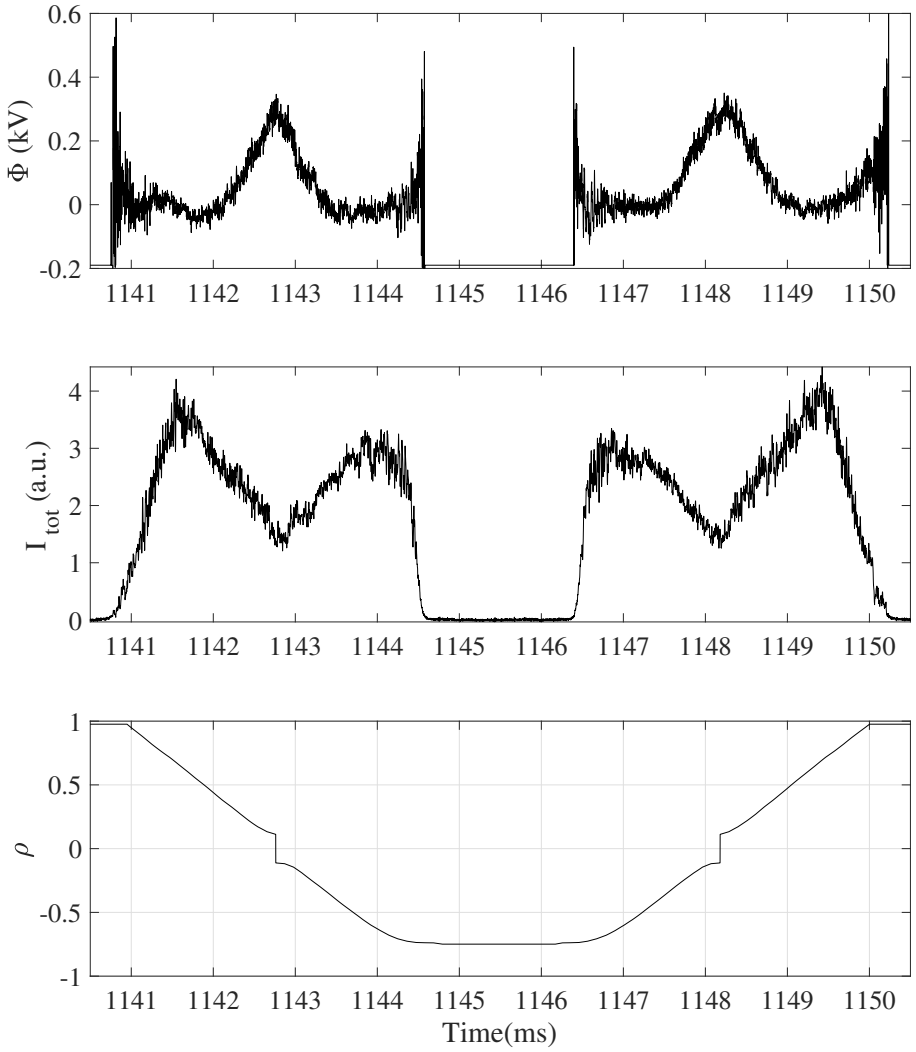

Figure 3. Example of data from the HIBP system during scanning operation. Top: Φ. Centre: $I_{\rm tot}$. Bottom: reconstructed normalized radius, ρ. Discharge 18907.

3.1. Spatiotemporal mapping of turbulent structures

The bottom panel of Fig, 4 shows the time evolution of the line average electron density, $\overline{n_e}$, in units of 10^{19} m^{-3} (as measured by the interferometer) in a particular discharge corresponding to the magnetic configuration 100_42_63. The density is initially low and is raised by means of the gas puffing system, crossing the mentioned critical density value of $\overline{n_e} \simeq 0.6 \cdot 10^{19}$ m^{-3}, resulting in a transition from electron root to ion root conditions. Later, the density is lowered again, resulting in a back transition.

We calculated the intermittence parameter $C(1)$ by subdividing the time trace $\Phi(t)$ in intervals of length $\Delta t = 0.1$ ms (2000 points), and applying the procedure described in Section 2.3 to each interval. Each value $C(1)$ obtained is associated with the mean time and the mean normalized radius ρ corresponding to the interval. Due to the scanning speed (cf. Fig. 3), the corresponding radial resolution is $\Delta\rho \simeq 0.05$.

The top panel of Fig, 4 shows the reconstructed spatiotemporal map of $C(1)$ for Φ in a discharge corresponding to the magnetic configuration labelled 100_42_63. Black slanted lines indicate the spatiotemporal trajectory of the location of the sampling volume during scanning. The 2-D colormap represents $C(1)$ after interpolation in time and space, using natural neighbor interpolation. As explained in Section 2.3, due to the fact that the plasma is rotating while the sampling volume is scanned, the graph reveals a mixture between the poloidal and temporal structure of the turbulence, which explains part of the variability of this and the next figure.

As noted in Section 2.3, minima of $C(1)$ tend to occur at locations and times where relatively strong (dominant) monofractal turbulent structures are formed. The line average electron density trace in the bottom panel shows a clear increase of fluctuations at the root transition times. This has been studied to some extent in previous work [25]. The top panel shows minima (blue) at these times. Thus, this figure allows a clear identification of the radial location of the turbulence causing the fluctuations in the time trace of $\overline{n_e}$, namely, $\rho \simeq 0.6$. In previous work, the fluctuation bursts occurring at the root transitions were identified as being due to acoustic modes in the gradient region, possibly coupled to MHD modes [25]. Indeed, in view of the known vacuum iota profile, it is likely that modes associated with the 11/7 and possibly also the 14/9 rational surfaces are involved.

The radial positions of the minima of $C(1)$ do not coincide exactly with the calculated position of the main rational surfaces. Apart from the fact that there may be small reconstruction errors in the positions of the various relevant quantities, the mode structures associated with a rational surface (and its helicity) do not need to coincide with the location of the rational surface itself, as explained in Section 2.3. In addition, interactions between modes associated with different rational surfaces may lead to deformations of the mode shape.

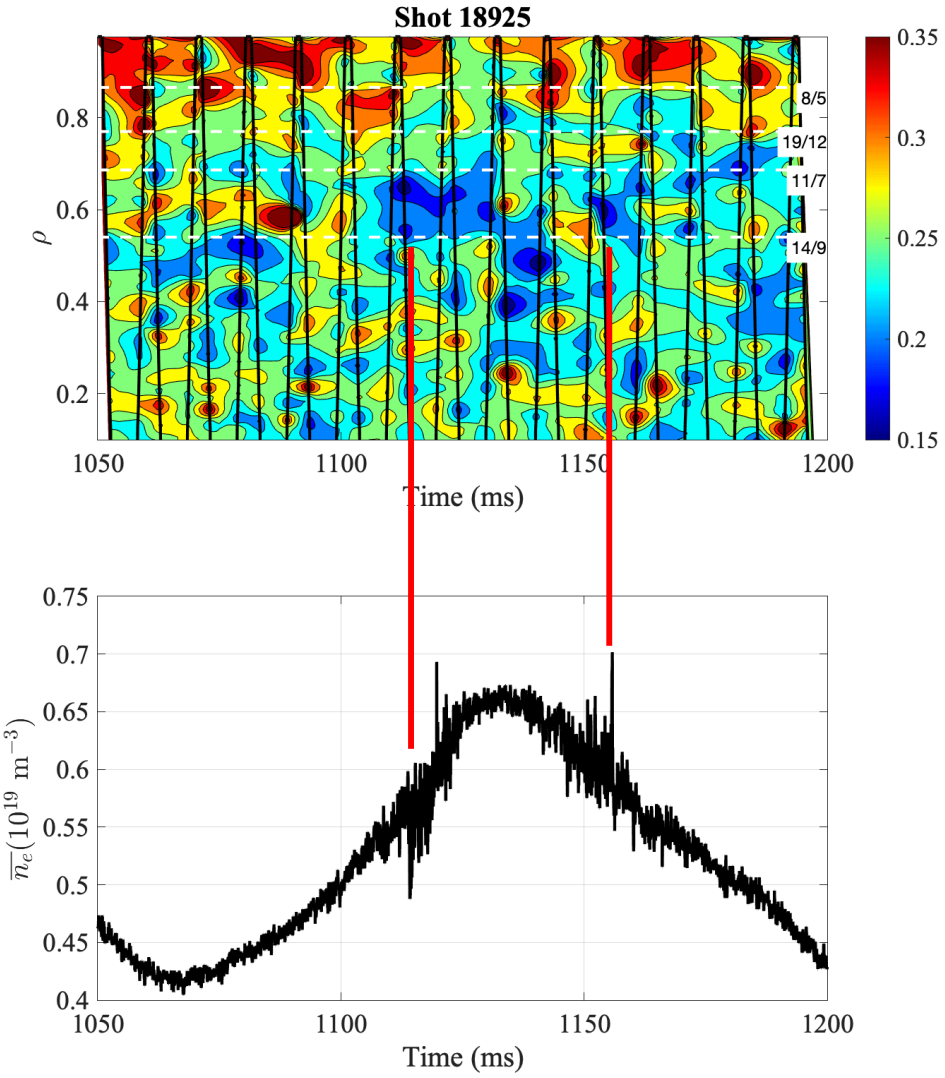

Figure 4. Top: spatiotemporal reconstruction of $C(1)$ for Φ from an ECRH heated discharge using fast scanning. Black slanted lines indicate the spatiotemporal trajectory of the location of the sampling volume during scanning. The 2-D colormap represents $C(1)$ after interpolation in time and space. Bottom: evolution of the line average density, $\overline{n_e}$. Red vertical lines are meant to guide the eye. Configuration 100_42_63.

The top panel of Fig, 5 shows the reconstructed spatiotemporal pattern of $C(1)$ for Φ in a discharge corresponding to the magnetic configuration labelled 100_46_65. The description of this figure is essentially identical to that of the previous figure. Note, however, that here one observes a long-living 'trench' in the reconstructed $C(1)$ map at $\rho \simeq 0.65$, for the whole duration of the ion root (high density) phase. This trench appears to be associated with the 8/5 rational surface. Interestingly, the temporal variation of mode frequency (and hence rotation speed) observed in earlier work [24] appears to match the temporal variation of the radial position of the 'trench' seen here (the cited reference shows the spectrogram of another discharge from this same series, closely similar to this one). Thus, the variation of the magnetic frequency (first up and then down) and the radial position of the intermittence trench (first outward and then inward) are clearly correlated, so that the frequency change of the rotating magnetic mode can likely be explained as a change of radial position of the mode in a more or less fixed background poloidal velocity profile. In the time interval 1140–1160 ms, a second trench is visible, associated with the rational 13/8. The corresponding magnetic activity has indeed been identified as corresponding to $m = 8$ in previous work [24].

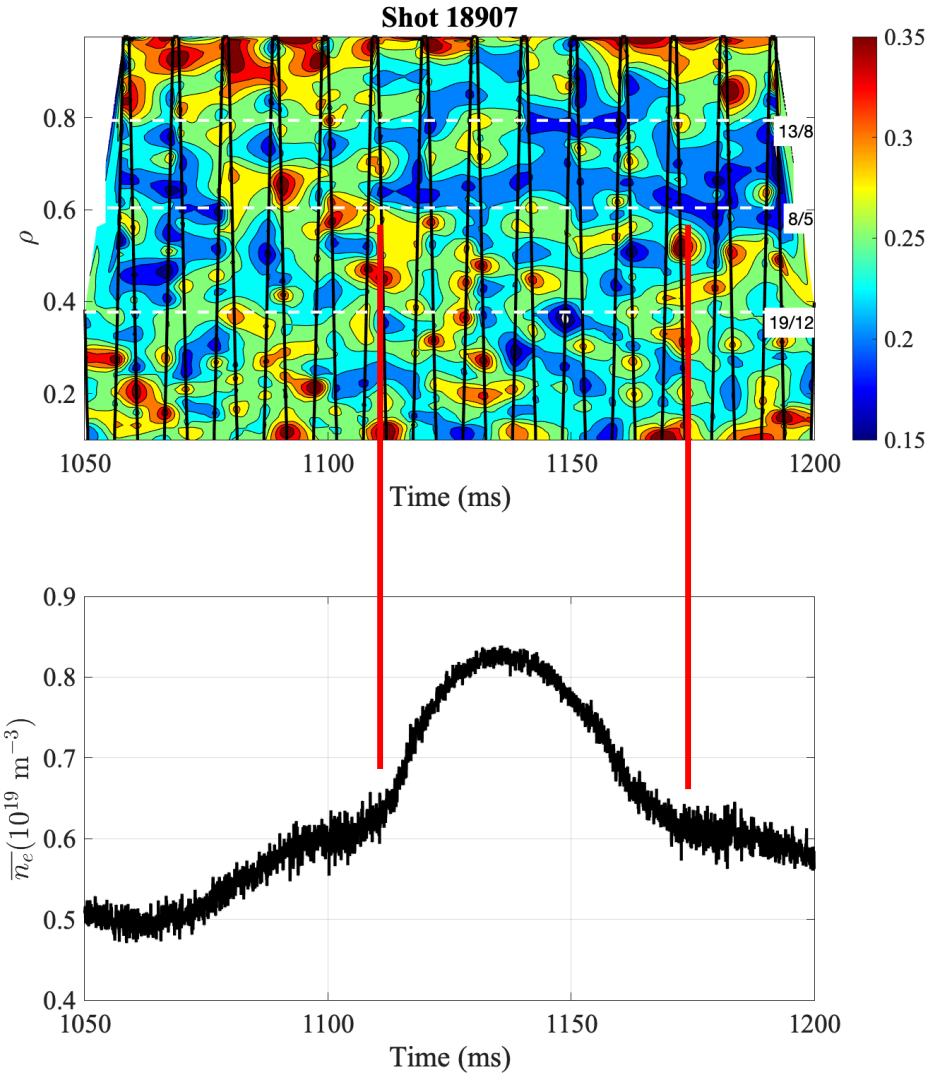

Figure 5. Top: spatiotemporal reconstruction of $C(1)$ for Φ from an ECRH heated discharge using fast scanning. Black slanted lines indicate the spatiotemporal trajectory of the location of the sampling volume during scanning. The 2-D colormap represents $C(1)$ after interpolation in time and space. Bottom: evolution of the line average density, $\overline{n_e}$. Red vertical lines are meant to guide the eye. Configuration 100_46_65.

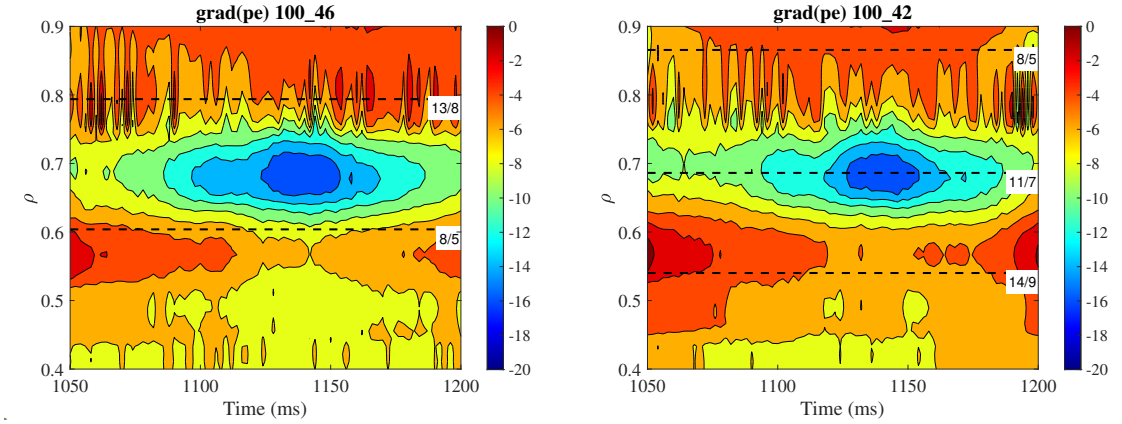

Figure 6. Radial pressure gradient $\nabla_r p_e$ (Pa/m), obtained by combining information on the n_e profile from interferometry and reflectometry [25] and information on the T_e profile from ECE.

In [25] we reconstructed the temporal evolution of the electron density n_e for these discharges, based on a Bayesian technique, combining diagnostic information from interferometry and reflectometry. The evolution of the electron temperature T_e could be recovered from ECE measurements. By combining this information, the evolution of the electron pressure p_e is obtained. The radial resolution offered by the ECE measurements is limited (12 points along the radial direction), so that only large-scale profile structures are detectable. The pressure evolves little over the time window of interest, as any increase of n_e is largely compensated by a corresponding drop in T_e, so that the central pressure is increased only mildly in the ion root phase (by 10–20%). Fig. 6 shows the mean evolution of the radial pressure gradient, $\nabla_r p_e$, in the two configurations studied. For $\rho \gtrsim 0.8$, T_e is low and experimental noise is significant, so the gradient is unreliable in this region. It is rather interesting to note that the pressure gradient steepens considerably (blue colors) during the times and in the radial region where the intermittence shows persistent minima (cf. Figs. 4 and 5).

3.2. Topology of the turbulent structures

The rotation velocity of the plasma has been estimated in previous work, based on the frequency of magnetic oscillations and Doppler reflectometry measurements [24]. Its order of magnitude is 2000 m/s in the region of interest (cf. also Fig. 7 below). If the poloidal plasma circumference at $\rho = 0.6$ equals $L = 2\pi\rho a \simeq 0.75$ m, the rotation frequency is typically $\omega \simeq 3$ kHz, and a poloidal rotation is completed in about 0.3 ms. Thus, given that scans are spaced by 5 ms in the fast scan experiments, the plasma typically completes various rotations between scans, and individual turbulent structures cannot be followed in time. However, if the nature of turbulence at a given location is persistent due to local characteristics (namely, the magnetic structure, i.e., MHD activity associated with a low order rational surface), this is detectable, as shown above.

To convert the spatiotemporal map obtained in Fig. 5 of Section 3.1 into a topological spatial map, plasma rotation has to be taken into account. As $\omega(r,t) = \dot{\theta}(r,t)$, one has

$$\theta = \int_{t_0}^{t} \omega(r,\tau) d\tau \tag{1}$$

If the rotation frequency ω were constant in time, one could simplify this as $\theta = \omega(r)(t - t_0)$. However, ω is neither constant in time nor space.

Thanks to the scanning operation, the plasma potential $\Phi(r,t)$ is known [16]. One has $E_r \simeq -\nabla\Phi$ (ignoring second-order geometric effects), and, assuming rotation is dominated by the $E \times B$ term, $v_\theta = E_r/B$; finally, $\omega = v_\theta/L$, where L is the poloidal circumference, $L \simeq 2\pi\rho a$. Using this, one can therefore make a good estimate of $\omega(r,t)$, needed to perform a reconstruction of the spatial map of $C(1)$. In doing so, we will use the approximations $B = 1$ T and $a = 0.2$ m.

Fig. 7 shows the reconstructed Φ and E_r. Some spatiotemporal smoothing was applied to Φ, mainly to reduce noise in E_r.

The poloidal angle θ, resulting from Eq. 1, is shown in Fig. 8. We have selected a reference time $t_0 = 1150$ ms, whose value is not critical but should lie in the region of interest. Generally speaking, plasma rotation is extremely fast, so that θ rapidly acquires very large positive or negative values. However, due to the inversion of the radial electric field E_r, associated with the root transition, there are specific radial and temporal moments when θ remains relatively small, i.e., plasma rotation and E_r are small. By selecting only data from regions where $-\pi \leq \theta \leq \pi$, we can thus recover the radial-poloidal mapping of $C(1)$, using the mapping $(\rho,t) \rightarrow (\rho,\theta)$, to convert the spatiotemporal map $C1(\rho,t)$ (cf. Fig. 5) to a topological map $C1(\rho,\theta)$.

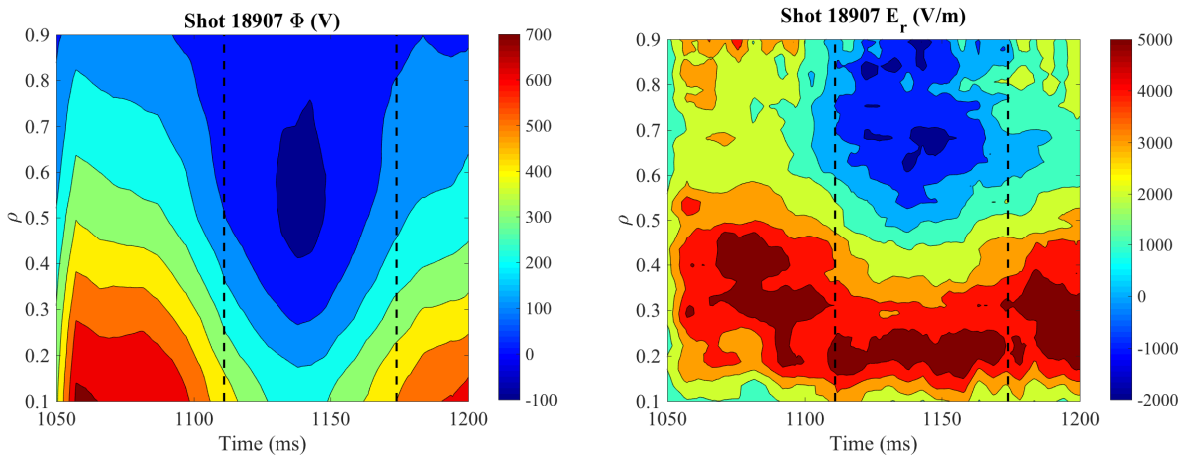

Figure 7. Spatiotemporal reconstruction of Φ and E_r for an ECRH heated discharge using fast scanning. Vertical dashed lines indicate the same times as the vertical lines included in Fig. 5.

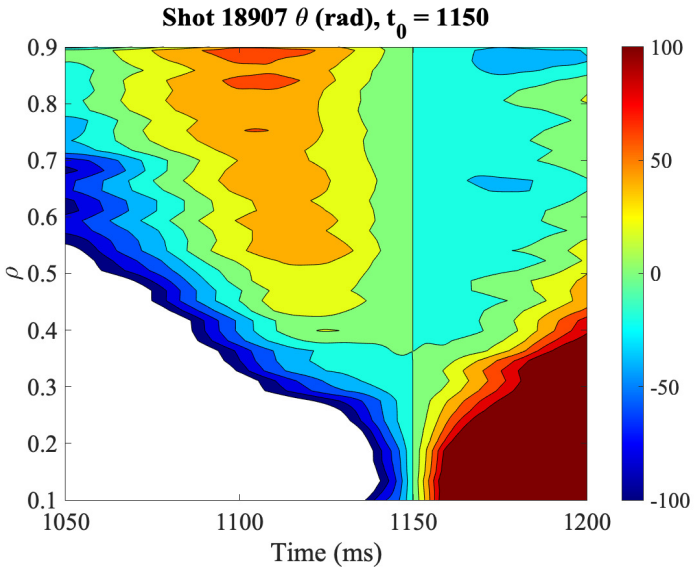

Figure 8. Spatiotemporal reconstruction of θ for an ECRH heated discharge using fast scanning.

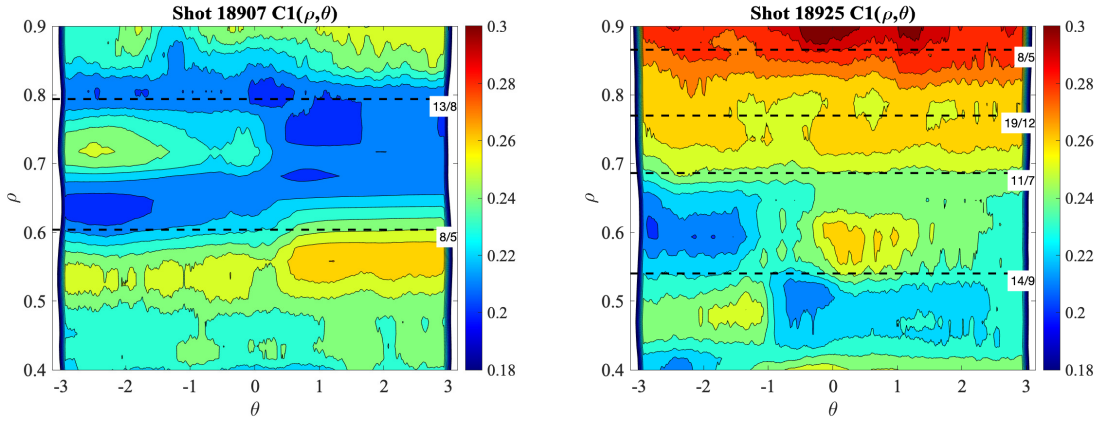

Figure 9. Twodimensional spatial reconstruction of $C1(\rho,\theta)$ for an ECRH heated discharge using fast scanning. Left: configuration '100_46_65'; $t_0 = 1150$ ms (discharge 18907). Right: configuration '100_42_63'; $t_0 = 1145$ ms (discharge 18925).

The result is shown in Fig. 9 (some smoothing has been applied). Due to the fact that only small values of θ have been used for this reconstruction, the poloidal resolution is low. In the case of discharge 18907 (left), the modes associated with the 8/5 and 13/8 rational surfaces resonate, as the minima of $C(1)$ tend to line up in terms of poloidal angle. This is consistent with the bicoherence analysis of [24]. Also in the case of discharge 18925 (right), obtained in a similar manner, the relative importance of the radial minima of $C(1)$ near important low order rational surfaces (here: 14/9) is clear. In this case, the mode appears to be radially asymmetric (odd) with respect to the rational surface. Something similar could be said, although less clearly, for the modes associated with the 8/5 and 13/8 modes in discharge 18907; this could be due to a certain degree of mixing between odd and even mode components.

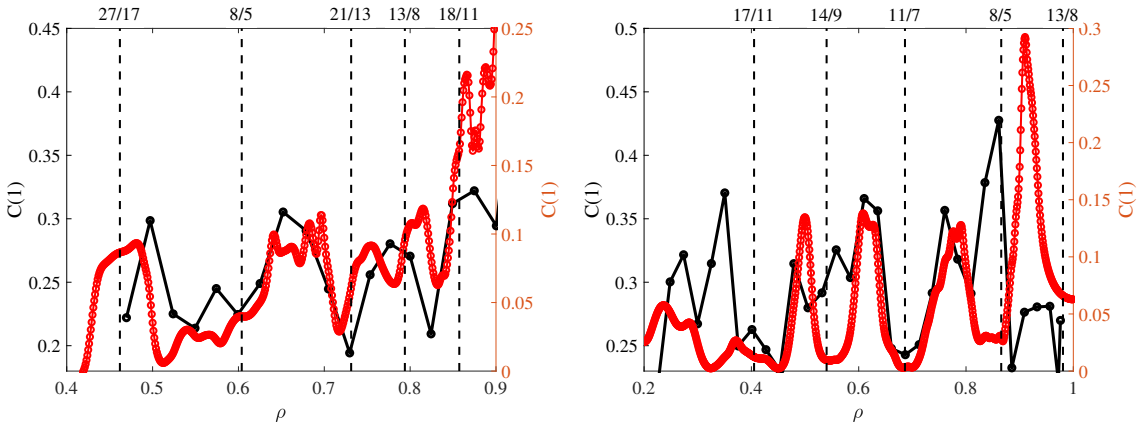

Figure 10. Experimental profiles of intermittence (black dots), compared to profiles from the numerical model (red dots). Left: configuration 100_46_65; right: configuration 100_42_63.

4. Comparison with model calculations

We have run the R-MHD model briefly described in Section 2.4 for the two TJ-II magnetic configurations considered here, 100_42_64 and 100_46_64. The model provides simulated fluctuations of the potential Φ on a very fast time scale, of the order of a few tens of microseconds. Since the poloidal rotation of the plasma is slow compared to this time scale, it is possible to sample the simulated fluctuations at various small intervals of the poloidal angle θ, thus obtaining simulated measurements of Φ at several poloidal positions and radii. We then apply the procedure to estimate the intermittence (cf. Section 2.3) to those simulated measurements $\Phi(\rho, \theta, t)$ to obtain $C(1)$ at different radial and poloidal locations.

Next, it is possible to compare the resulting radial profiles of $C(1)$ at several poloidal locations to the radial profiles obtained in the experiment. This procedure is necessary as the correspondence between the poloidal angle of the cylindrical model and the experimental poloidal angle is unclear.

Examples of such comparisons are shown in Fig. 10. In a broad range of ρ (from about 0.4 to about 0.8), we find a high degree of coincidence between (a) the positions of low-order rational surfaces, (b) minima in the experimental profiles of $C(1)$, and (c) minima in the profiles of $C(1)$ calculated from the numerical model.

For $\rho > 0.85$, $C(1)$ has a tendency to rise sharply. The causes for this observation are not fully known, but could be related to the fact that the rotational transform profile steepens in the edge region, implying a larger density of (interacting) rational surfaces, leading to an increase of intermittence. Edge radial electric fields may also play a part [14].

As the model yields $C(1)$ as a function of ρ and θ, it is possible to plot the 2-D turbulent structures for these two configurations, similar to the reconstructions made in Section 3.2. Fig. 11 shows the 2-D plots of $C(1)$ as a function of the radial

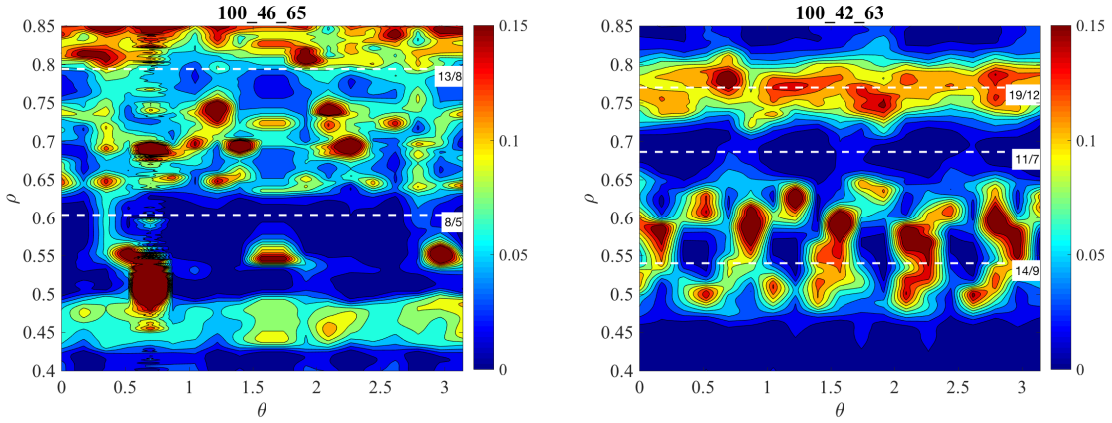

Figure 11. Radial-poloidal intermittence map obtained from the R-MHD model. Left: configuration 100_46_65. Right: configuration 100_42_63.

and poloidal coordinates for the two discharges, corresponding to the configurations 100_46_65 and 100_42_63. The vortex structures correspond to minima of $C(1)$, the dark blue regions. One observes that these structures are either at the rational surfaces or nearby, depending on the symmetry of the components of the main helicities with respect of the rational radial position. At a given rational surface, the number of minima of $C(1)$ is consistent with the m value associated with the surface.

As mentioned above, these numerical results are not a detailed simulation of the plasma, so no direct comparison is posible with experiment, which in any case would be difficult due to the temporal variability of turbulence. As noted, the experimental reconstructions shown in Section 3.2 do not offer sufficient poloidal resolution to properly resolve the poloidal structure.

5. Discussion and conclusions

This work presents the first estimations ever of the degree of intermittence of the plasma potential Φ, calculated from experimental data obtained over most of the plasma radius by a HIBP system in the TJ-II stellarator.

The present work shows that core potential fluctuations possess a property (intermittence) that varies in a significant way with plasma conditions (electron or ion root, and the transition between the two). The formation of radial minima of $C(1)$ in relation to the electron-ion root transition is observed. The persistence of the minima of $C(1)$ over various successive scans of the HIBP system attests to their physical significance and reproducibility.

The minima are clearly associated with low-order rational surfaces. In Fig. 5, a 'trench' of low values of $C(1)$ is observed, close to the expected location of the important 8/5 rational surface in the ion root phase. Comparing this with the analysis of magnetic activity and mode numbers m performed in previous work using Mirnov coils [24], we conclude that this trench is without any doubt related to the 8/5 mode. Moreover, the temporal variation of the mode frequency detected using the Mirnov coils matches the temporal variation of the radial location of the intermittence 'trench'. This suggests that during the ion root phase, with continuously varying electron density, the mode location moves radially in accordance with the varying density, and therefore experiences a varying poloidal rotation velocity (cf. the velocity profiles deduced in [24]), which provides an explanation for the varying mode frequency. This sequence of events provides definitive experimental proof of the association between intermittence minima and mode location.

Further evidence is obtained by estimating the electron pressure gradient, $\nabla_r p_e$, from experimental profile measurements. Fig. 6 shows how the pressure gradient steepens considerably at the times and radial locations where the intermittence displays minimum values. It is therefore reasonable to assume that these minima are associated with pressure gradient driven modes. In the future, this type of study might even allow the experimental determination of the critical pressure gradient to trigger these modes, if any.

From the measured low-frequency (background) evolution of the potential, $\Phi(\rho, t)$, we could recover the radial electric field $E_r(\rho, t)$ and hence the poloidal rotation velocity $v_\theta(\rho, t)$ (assuming that the $E \times B$ velocity dominates plasma rotation). Using this knowledge, we could convert the spatiotemporal intermittence into an approximate topological (radial-poloidal) map of intermittence. This unique reconstruction further clarified the topological structure of turbulence.

Results obtained from an R-MHD model were compared to the experimental results. It was found there is good agreement of the experimental and model minima of $C(1)$ over a large part of the plasma radius, and that these minima tend to align with major low order rationals. The topological reconstruction of $C(1)$ reflected the expected poloidal structure of MHD modes, radially associated with the corresponding rational and with

the corresponding poloidal periodicity. Comparing with the experimental topological reconstructions, we note that the experimental radial structure was roughly as expected, wheres the experimental poloidal resolution was insufficient to resolve the periodicity.

In conclusion, near low order rational surfaces, modes with the corresponding helicity may dominate fluctuations if they are driven (e.g., due to a locally steep pressure gradient), leading to a reduction of the degree of multifractality and hence the intermittence parameter [13]. Low-order modes tend to dominate over higher order modes, hence the intermittence parameter tends to decrease mainly near low-order rational surfaces. Such modes may facilitate the formation of turbulent vortices even in the absence of fully-formed magnetic islands. This may lead to 'trapping' and therefore affect radial particle and heat transport [7]. Through this mechanism, low-order rational surfaces are expected to affect transport.

Finally, we have shown that important information on turbulence in core plasmas is contained in data from existing diagnostics (like ECE and HIBP), but that advanced analysis techniques based on quantities like the Transfer Entropy [7] and the intermittence [13, 14] are needed to extract it. Thus, these nonlinear techniques provide access to information that is not easily available by other means, and may be used to shed light on the interaction between turbulence and background profiles. We would therefore like to suggest that these techniques should be used more generally to improve our understanding of anomalous transport.

Acknowledgements

This work has been carried out within the framework of the EUROfusion Consortium and has received funding from the Euratom research and training programme 2014-2018 and 2019-2020 under grant agreement No. 633053. The views and opinions expressed herein do not necessarily reflect those of the European Commission. Research sponsored in part by the *Ministerio de Ciencia, Innovación y Universidades* of Spain under project Nos. PGC2018-097279-B-I00 and PID2019-110734RB-I00. The work of the Kurchatov team was funded by the Russian Science Foundation under Project 19-12-00312 and the work of A.V. Melnikov was partly supported by the Competitiveness program of NRNU MEPhI. BAC gratefully acknowledges support for the research from the DOE office of Fusion Energy under U.S. Department of Energy Contract DE-SC0018076.

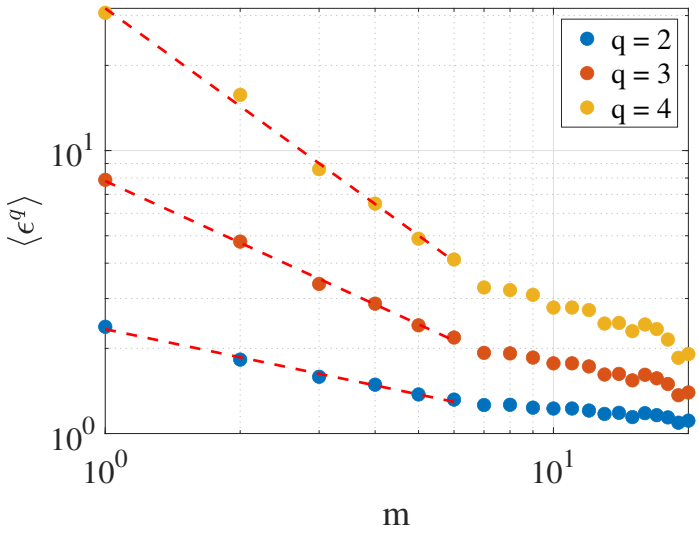

Figure A1. Example curves of $\langle \epsilon(n,i)^{\mathfrak{q}} \rangle$ (dots, q values are specified in the legend). Fits to the first $n_1 = 6$ points of each curve are indicated by red dashed lines.

Appendix A. Calculation of the intermittence parameter

In this article, we use the methods for calculating the intermittence of temporal signals described in Refs. [8, 9, 11], which we summarize here for convenience. Given a time series $X = \{x_i, i = 1, \ldots, N\}$ that has been sampled at a constant sampling rate, we calculate the measure

$$\epsilon(1,i) = \frac{(x_i - \langle x_i \rangle)^2}{\langle (x_i - \langle x_i \rangle)^2 \rangle}, \qquad i = 1, \ldots, N, \tag{A.1}$$

where $\langle x_i \rangle = (\sum_{i=1}^{N} x_i)/N$. This measure can be averaged over subblocks of data of length $n < N$, as follows:

$$\epsilon(n,i) = \frac{1}{n} \sum_{j=0}^{n-1} \epsilon(1, i+j). \tag{A.2}$$

We then calculate the $\mathfrak{q}$-moments, $\langle \epsilon(n,i)^{\mathfrak{q}} \rangle$. In a given range of n-values, these moments are expected to scale like [26]:

$$\langle \epsilon(n,i)^{\mathfrak{q}} \rangle \propto n^{-K(\mathfrak{q})}, \tag{A.3}$$

where $K(1) \equiv 0$. An example is shown in Fig. A1. If the time series X is monofractal, the function $K(\mathfrak{q})$ is asymptotically linear in $\mathfrak{q}$, otherwise the series is multifractal.

Since we are interested in the turbulent (high frequency) characteristics of the fluctuations, we determine $K(\mathfrak{q})$ from a linear fit of a set of values of $\log\langle \epsilon^{\mathfrak{q}} \rangle$ versus $\log n$, for a range of values of $n = 1, \ldots, n_1$, where n_1 is small, e.g. $n_1 = 6$, and for a few values of $\mathfrak{q}$ (see below). The parameter $K(\mathfrak{q})$ is robust in the sense that the choice of n_1 is not critical, although ocular inspection of the $\log\langle \epsilon^{\mathfrak{q}} \rangle$ versus $\log n$ curves is recommended to check that the curves behave as a power law for small n (cf. Fig. A1).

The parameter $C(\mathbb{q})$ is defined as [26]:

$$C(\mathbb{q}) = \frac{K(\mathbb{q})}{\mathbb{q}-1}. \tag{A.4}$$

Of special interest is the so-called 'intermittence parameter' $C(1)$, which which must be calculated using L'Hôpital's rule:

$$C(1) = \left.\frac{dK(\mathbb{q})}{d\mathbb{q}}\right|_{\mathbb{q}=1} \tag{A.5}$$

due to the singularity of Eq. A.4 at $\mathbb{q} = 1$. Its value ranges from 0, for a monofractal time series, to 1.

To find the intermittence parameter $C(1)$, Eq. (A.5), one needs to calculate $K(\mathbb{q})$ values for various values of $\mathbb{q} \neq 1$ and use those to estimate $C(1)$. It is not possible to obtain $K(\mathbb{q})$ for $\mathbb{q} < 1$ due to the absence of a clear linear scaling region according to Eq. (A.3). Using finite $\mathbb{q} > 1$ values, one can use the following three approximate expressions to estimate the slope at $\mathbb{q} = 1$ obtained by Taylor expansion in $\mathbb{q}$ with the condition K(1)=0:

$$\begin{aligned}
C_0(1) &= \left.\frac{dK}{d\mathbb{q}}\right|_{\mathbb{q}=1} = 4K(1.5) - K(2) \\
C_1(1) &= \left.\frac{dK}{d\mathbb{q}}\right|_{\mathbb{q}=1} = 2K(2) - \frac{1}{2}K(3) \\
C_2(1) &= \left.\frac{dK}{d\mathbb{q}}\right|_{\mathbb{q}=1} = \frac{8}{3}K(1.5) - \frac{1}{6}K(3)
\end{aligned} \tag{A.6}$$

These three estimates of the derivative yield similar results for $C(1)$ [13]. In this paper, we estimate $C(1)$ using $C_1(1)$.

ORCID codes

B.P. van Milligen: ORCID 0000-0001-5344-6274
A.V. Melnikov: ORCID 0000-0001-6878-7493
B.A. Carreras: ORCID 0000-0001-7921-4690
L. García: ORCID 0000-0002-0492-7466
C. Hidalgo: ORCID 0000-0002-0736-7855
J.L. de Pablos: ORCID 0000-0002-3850-0196

References

[1] U. Stroth. A comparative study of transport in stellarators and tokamaks. *Plasma Phys. Control. Fusion*, 40:9, 1998. doi:10.1088/0741-3335/40/1/002.

[2] P. Helander, C.D. Beidler, T.M. Bird, M. Drevlak, Y. Feng, R. Hatzky, F. Jenko, R. Kleiber, J.H.E. Proll, Yu. Turkin, and P. Xanthopoulos. Stellarator and tokamak plasmas: a comparison. *Nucl. Fusion*, 54:124009, 2012. doi:10.1088/0741-3335/54/12/124009.

[3] R. Balescu. *Aspects of anomalous transport in plasmas*. Institute of Physics, Bristol, 2005.

[4] A V Melnikov, L I Krupnik, E Ascasibar, A Cappa, A A Chmyga, G N Deshko, M A Drabinskij, L G Eliseev, C Hidalgo, P O Khabanov, S M Khrebtov, N K Kharchev, A D Komarov, A S Kozachek, S E Lysenko, A Molinero, J L de Pablos, M V Ufimtsev, and V N Zenin. ECRH effect on the electric potential and turbulence in the TJ-II stellarator and T-10 tokamak plasmas. *Plasma Phys. Control. Fusion*, 60:084008, 2018. doi:10.1088/1361-6587/aac97f.

[5] A. Melnikov. *Electric potential in toroidal plasmas*. Springer Nature Switzerland AG, 2019.

[6] Ridhima Sharma, Philipp Khabanov, Alexander Melnikov, Carlos Hidalgo, Alvaro Cappa, A Chmyga, Leonid Eliseev, Teresa Estrada, Nikolai Khartchev, A. Kozachek, Lyudmila Krupnik, Artur Malaquias, Boudewijn van Milligen, Antonio Molinero, Jose Luis de Pablos, Ignacio Pastor, and V. Zenin. Measurements of 2D poloidal plasma profiles and fluctuations in ECRH plasmas using the Heavy Ion Beam Probe system in the TJ-II stellarator. *Phys. Plasmas*, 27:062502, 2020. doi:10.1063/1.5142996.

[7] B.Ph. van Milligen, B. Carreras, L. García, and J. Nicolau. The radial propagation of heat in strongly driven non-equilibrium fusion plasmas. *Entropy*, 21(2):148, 2019. doi:10.3390/e21020148.

[8] C. Meneveau and K.R. Sreenivasan. Simple multifractal cascade model for fully developed turbulence. *Phys. Rev. Lett.*, 59:1424, 1987. doi:10.1103/PhysRevLett.59.1424.

[9] C. Meneveau and K.R. Sreenivasan. The multifractal nature of turbulent energy dissipation. *J. Fluid Mechanics*, 224:429, 1991. doi:10.1017/S0022112091001830.

[10] V.A. Sandborn. Measurements of intermittency of turbulent motion in a boundary layer. *J. Fluid Mechanics*, 6(2):221, 1959. doi:10.1017/S0022112059000581.

[11] B.A. Carreras, V.E. Lynch, D.E. Newman, R. Balbín, J. Bleuel, M.A. Pedrosa, M. Endler, B. van Milligen, E. Sánchez, and C. Hidalgo. Intermittency of plasma edge fluctuation data: Multifractal analysis. *Phys. Plasmas*, 7(8):3278, 2000. doi:10.1063/1.874193.

[12] B.Ph. van Milligen, U. Hoefel, J.H. Nicolau, M. Hirsch, L. García, B.A. Carreras, C. Hidalgo, and the W7-X Team. Study of radial heat transport in W7-X using the transfer entropy. *Nucl. Fusion*, 58(7):076002, 2018. doi:10.1088/1741-4326/aabf5d.

[13] B.A. Carreras, L. García, J.H. Nicolau, B.Ph. van Milligen, U. Hoefel, M. Hirsch, and the TJ-II and W7-X Teams. Intermittence and turbulence in fusion devices. *Plasma Phys. Control. Fusion*, 62:025011, 2020. doi:10.1088/1361-6587/ab57f9.

[14] B. Ph. van Milligen, B.A. Carreras, L. García, and C. Hidalgo. The localization of low order rational surfaces based on the intermittence parameter in the TJ-II stellarator. *Nucl. Fusion*, 60:056010, 2020. doi:10.1088/1741-4326/ab79cc.

[15] C. Hidalgo, C. Alejaldre, A. Alonso, J. Alonso, L. Almoguera, F. de Aragón, E. Ascasíbar, A. Baciero, R. Balbín, E. Blanco, J. Botija, B. Brañas, E. Calderón, A. Cappa, J.A. Carmona, R. Carrasco, F. Castejón, J.R. Cepero, A.A. Chmyga, J. Doncel, N.B. Dreval, S. Eguilior, L. Eliseev, T. Estrada, J.A. Ferreira, A. Fernández, J.M. Fontdecaba, C. Fuentes, A. García, I. García-Cortés, B. Gonçalves, J. Guasp, J. Herranz, A. Hidalgo, R. Jiménez, J.A. Jiménez, D. Jiménez-Rey, I. Kirpitchev, S.M. Khrebtov, A.D. Komarov, A.S. Kozachok, L. Krupnik, F. Lapayese, M. Liniers, D. López-Bruna, A. López-Fraguas, J. López-Rázola, A. López-Sánchez, E. de la Luna, G. Marcon, R. Martín, K.J. McCarthy, F. Medina, M. Medrano, A.V. Melnikov, P. Méndez, B. van Milligen, I.S. Nedzelskiy, M. Ochando, O. Orozco, J.L. de Pablos, L. Pacios, I. Pastor, M.A. Pedrosa, A. de la Peña, A. Pereira, A. Petrov, S. Petrov, A. Portas, D. Rapisarda,

L. Rodríguez-Rodrigo, E. Rodríguez-Solano, J. Romero, A. Salas, E. Sánchez, J. Sánchez, M. Sánchez, K. Sarksian, C. Silva, S. Schchepetov, N. Skvortsova, F. Tabarés, D. Tafalla, A. Tolkachev, V. Tribaldos, I. Vargas, J. Vega, G. Wolfers, and B. Zurro. Overview of TJ-II experiments. *Nucl. Fusion*, 45:S266, 2005. doi:10.1088/0029-5515/45/10/S22.

[16] B.Ph. van Milligen, M.A. Pedrosa, C. Hidalgo, B.A. Carreras, T. Estrada, J.A. Alonso, J.L. de Pablos, A. Melnikov, L. Krupnik, L.G. Eliseev, and S.V. Perfilov. The dynamics of the formation of the edge particle transport barrier at TJ-II. *Nucl. Fusion*, 51:113002, 2011. doi:10.1088/0029-5515/51/11/113002.

[17] J.L. Velasco, J.A. Alonso, I. Calvo, and J. Arévalo. Vanishing neoclassical viscosity and physics of the shear layer in stellarators. *Phys. Rev. Lett.*, 109(13):135003, 2012. doi:10.1103/PhysRevLett.109.135003.

[18] B.Ph. van Milligen, J.H. Nicolau, L. García, B.A. Carreras, C. Hidalgo, and the TJ-II Team. The impact of rational surfaces on radial heat transport in TJ-II. *Nucl. Fusion*, 57(5):056028, 2017. doi:10.1088/1741-4326/aa611f.

[19] A.V. Melnikov, L.I. Krupnik, L.G. Eliseev, J.M. Barcala, A. Bravo, A.A. Chmyga, G.N. Deshko, M.A. Drabinskij, C. Hidalgo, P.O. Khabanov, S.M. Khrebtov, N.K. Kharchev, A.D. Komarov, A.S. Kozachek, J. Lopez, S.E. Lysenko, G. Martin, A. Molinero, J.L. de Pablos, A. Soleto, M.V. Ufimtsev, V.N. Zenin, A.I. Zhezhera, T-10 Team, and the TJ-II Team. Heavy ion beam probing-diagnostics to study potential and turbulence in toroidal plasmas. *Nucl. Fusion*, 57:072004, 2017. doi:10.1088/1741-4326/aa5382.

[20] Ph.O. Khabanov, L.G. Eliseev, A.V. Melnikov, M.A. Drabinskiy, C. Hidalgo, N.K. Kharchev, A.A. Chmyga, A.S. Kozachek, I. Pastor, J.L. de Pablos, A. Cappa, and V.P. Shevelko. Density profile reconstruction using HIBP in ECRH plasmas in the TJ-II stellarator. *Journal of Instrumentation*, 14:C09033, 2019. doi:10.1088/1748-0221/14/09/C09033.

[21] L. García, B.A. Carreras, V.E. Lynch, M.A. Pedrosa, and C. Hidalgo. Sheared flow amplification by vacuum magnetic islands in stellarator plasmas. *Phys. Plasmas*, 8(9):4111, 2001. doi:10.1063/1.1392996.

[22] L. García and B.A. Carreras. Identification and characterization of topological structures of turbulence in magnetic confined plasmas. *Plasma Phys. Control. Fusion*, 62:115013, 2020. doi:10.1088/1361-6587/abb53c.

[23] H.R. Strauss. Nonlinear, three-dimensional magnetohydrodynamics of noncircular tokamaks. *Phys. Fluids*, 19:134, 1976. doi:10.1063/1.861310.

[24] B.Ph. van Milligen, L. García, B.A. Carreras, M.A. Pedrosa, C. Hidalgo, J.A. Alonso, T. Estrada, and E. Ascasíbar. MHD mode activity and the velocity shear layer at TJ-II. *Nucl. Fusion*, 52:013006, 2011. doi:10.1088/0029-5515/52/1/013006.

[25] B.Ph. van Milligen, T. Estrada, R. Jiménez-Gómez, A. Melnikov, C. Hidalgo, J.M. Fontdecaba, L. Krupnik, L.G. Eliseev, S.V. Perfilov, and the TJ-II Team. A global resonance phenomenon at the TJ-II stellarator. *Nucl. Fusion*, 51:013005, 2011. doi:10.1088/0029-5515/51/1/013005.

[26] H.G.E. Hentschel and I. Procaccia. The infinite number of generalized dimensions of fractals and strange attractors. *Physica D*, 8(3):435, 1983. doi:10.1016/0167-2789(83)90235-X.